

## Hydrogen embrittlement at elevated temperature during low cycle fatigue of AISI 321 stainless steel



Citation for the original published paper (version of record):

Anilkumar, V., Wanjura, S., Kulawinski, D. et al (2026). Hydrogen embrittlement at elevated temperature during low cycle fatigue of AISI 321 stainless steel. Engineering Failure Analysis, 184. http://dx.doi.org/10.1016/j.engfailanal.2025.110307

N.B. When citing this work, cite the original published paper.

research.chalmers.se offers the possibility of retrieving research publications produced at Chalmers University of Technology. It covers all kind of research output: articles, dissertations, conference papers, reports etc. since 2004. research.chalmers.se is administrated and maintained by Chalmers Library

FISEVIER

Contents lists available at ScienceDirect

### **Engineering Failure Analysis**

journal homepage: www.elsevier.com/locate/engfailanal



## Hydrogen embrittlement at elevated temperature during low cycle fatigue of AISI 321 stainless steel

Vishnu Anilkumar <sup>a,b</sup>, Stefan Wanjura <sup>c</sup>, Dirk Kulawinski <sup>c</sup>, Frans Palmert <sup>d</sup>, Johan Ahlström <sup>a</sup>, Lars Nyborg <sup>a,b</sup>, Yu Cao <sup>a,b,\*</sup>

- a Department of Industrial and Materials Science, Chalmers University of Technology, Göteborg 412 96, Sweden
- <sup>b</sup> TechForH2 Excellence Centre, Chalmers University of Technology, Göteborg 412 96, Sweden
- <sup>c</sup> Siemens Energy Global GmbH & Co. KG, Mülheim an der Ruhr, Germany

#### ARTICLE INFO

# Keywords: Hydrogen embrittlement Strain-controlled low cycle fatigue Austenitic stainless steel Delta-ferrite

#### ABSTRACT

Adapting industrial gas turbines, which are traditionally fuelled by natural gas, to run on pure hydrogen or hydrogen-natural gas blends is critical for eliminating or lowering CO2 emissions in power generation. However, hydrogen embrittlement challenges the mechanical integrity of stainless steel 321, commonly used in fuel supply pipes. While deformation-induced martensite formation is widely recognized as a key factor contributing to hydrogen embrittlement in metastable austenitic stainless steels. The influence of delta-ferrite, temperature, and the type of mechanical loading have received less attention. In this study, AISI 321 stainless steel was thermally precharged in gaseous hydrogen with a pressure of 4.6 MPa at 350 °C for 672 h. Straincontrolled low cycle fatigue tests were performed at room temperature and at 120 °C in a hydrogen atmosphere at the same pressure. Emphasis was placed on fractographic analysis and phase evolution during deformation. A reduction in fatigue life was observed in hydrogen atmosphere at both temperatures. When compared to ambient temperature, fatigue life is enhanced at 120 °C in air due to the absence of martensite transformation. Nonetheless in hydrogen, this improvement is compromised by delta ferrite. Its phase boundary acts as a place for faster crack initiation and propagation, resulting in embrittlement. The underlying hydrogen embrittlement mechanisms is discussed. These findings provide crucial insight for material selection in hydrogen-fuelled gas turbines, underscoring the need to minimize delta-ferrite content to enhance the resistance to HE up to 120 °C.

#### 1. Introduction

The combustion of hydrogen ( $H_2$ ) to achieve carbon–neutral power generation using industrial gas turbines (IGTs) is attractive owing to IGTs high-power generation capacity, fuel flexibility and high efficiency [1]. In this context, equipping conventional IGT infrastructure for combustion of  $H_2$  is key in enabling economically viable energy transition. Austenitic stainless steel 321 (AISI 321), acclaimed for its superior corrosion resistance and weldability, is widely used in fuel supply pipes, combustor parts, and exhaust components of conventional IGTs [2]. The large strain range reversals induced by cyclic loading during gas turbine start-up and

E-mail address: yu.cao@chalmers.se (Y. Cao).

https://doi.org/10.1016/j.eng fail anal. 2025.110307

<sup>&</sup>lt;sup>d</sup> Siemens Energy AB, Finspång, Sweden

<sup>\*</sup> Corresponding author.

shutdown events make fatigue the dominant life-limiting damage mechanism for these components [3]. In addition, fuel supply pipes are exposed to temperatures above  $100\,^{\circ}$ C in service. Compatibility and reliability are of great importance in service conditions when exposed to high-pressure gaseous  $H_2$ .

Hydrogen embrittlement (HE) is a phenomenon in which the ductility and toughness of metallic materials is reduced due to hydrogen uptake, which may lead to premature failures. It is generally accepted that austenitic stainless steel is a material of choice in relevant applications owing to the low diffusivity of atomic hydrogen (H) in austenite with a face-centered cubic (FCC) structure [4]. However, metastable austenitic stainless steel, such as AISI 304, undergoes deformation-induced martensite (DIM) transformation, where austenite partially transforms to martensitic microstructure during deformation and contributes to transformation-induced plasticity (TRIP) [5]. Compared to austenite, the higher diffusivity and lower solubility of H in DIM lead to H accumulation at the phase boundaries, causing cracking [6,7]. It has been reported that thermal gaseous pre-charging with H<sub>2</sub> lowers the fatigue life of notched AISI 304 test bars during stress-controlled low cycle fatigue (LCF) tests in ambient conditions [8]. Fatigue cracks propagate along the interface of austenite and DIM. For notched AISI 304 with electrochemically charged H, an increased crack growth rate was also reported during stress-controlled fatigue tests in air at room temperature (RT). This was again correlated to the formation of DIM near the crack tip with increased local H concentration. Here, the prime cause of HE is reported to be the diffusion and accumulation of H to the crack tip, leading to altered slip deformation. The formation of DIM facilitates H diffusion and consequently increases its concentration [9].

Until now, a multitude of HE studies have been performed in metastable austenitic stainless steels focusing on LCF at RT. The effects of increased testing temperatures in strain-controlled LCF are not well understood. It is well known that deformation-induced martensitic transformation is closely related to the temperature, and the fraction of DIM decreases with temperature. When the temperature is above  $M_d$ , the formation of DIM is impossible [10]. This temperature-induced stability of austenite improves the HE resistance of AISI 304L during tensile testing. Consequently, it is commonly inferred that these steels regain ductility at temperatures unfavourable for martensite formation [11].

However, HE susceptibility can also be worsened by the presence of phases that are prone to embrittlement and remain stable at temperatures unfavourable for DIM formation. An example is delta-ferrite ( $\delta$ -ferrite), which commonly forms during casting and can be retained at room temperature after thermo-mechanical processing and subsequent solution annealing. In low-nickel alloyed austenitic stainless steels such as AISI 304, a  $\delta$ -ferrite content of approximately 2 % is typically observed in solution annealed state [12,13]. After thermal pre-charging with H<sub>2</sub>,  $\delta$ -ferrite phase boundaries within the austenite matrix in AISI 304L have been found to act as sites for crack initiation during tensile testing in air at RT [12]. Similar behaviour was observed in stress-controlled LCF tests conducted in H<sub>2</sub> atmosphere at RT, where cracks initiated along the phase boundaries of  $\delta$ -ferrite in AISI 304. It has also been found in the same study that  $\delta$ -ferrite accelerated fatigue crack growth in high  $\delta$ -ferrite containing AISI 304 compared to  $\delta$ -ferrite free AISI 304 in solutionannealed state, and the cracks propagate along the phase boundaries [14].

As a metastable austenitic stainless steel, AISI 321 also undergoes deformation-induced martensite transformation [15,16], similar to AISI 304. Regarding HE, the investigation on AISI 321 has been rather limited. It has been found that AISI 321 is prone to cracking in service when exposed to hydrogen-containing hot gas at high pressure [17]. In lab-scale tests, hydrogen has often been introduced into the steel using the cathodic electrochemical method. Hydrogen embrittlement is then examined by tensile testing at room temperature, and correlated to the formation of DIM [18–20]. Nevertheless, the testing conditions favoured the formation of DIM, making it difficult to isolate the specific influence of  $\delta$ -ferrite. Furthermore, current understanding of HE susceptibility in austenitic stainless steels across a broad temperature range ( $-150\,^{\circ}\text{C}$  to  $+150\,^{\circ}\text{C}$ ) primarily derives from tensile test data and emphasize the role of reduced martensite formation [11].

Considering the application conditions of AISI 321 as fuel supply pipes in hydrogen-powered gas turbines, a comprehensive investigation of strain-controlled LCF behaviour under conditions of pressurized hot hydrogen gas is urgently required. Such investigation is particularly critical due to the fundamental differences in damage evolution between LCF and tensile tests, as well as the stability of  $\delta$ -ferrite at elevated temperatures where martensitic transformation is not thermodynamically favoured. In this regard, this study aims to examine HE of AISI 321 containing  $\delta$ -ferrite by thermal pre-charging and subsequent strain-controlled in-situ LCF test in 4.6 MPa H<sub>2</sub> at both RT and 120 °C. The possible activation mechanisms of HE and the effect of  $\delta$ -ferrite have been discussed. The results from the study will play a crucial role in understanding HE in AISI 321 important for future materials selection.

#### 2. Material and methods

A commercial grade AISI 321 was used in this study. The hot rolled plate was solution annealed at 1050°C for 1 h followed by air quenching. The chemical composition of the as-received steel is listed in Table 1.

Test materials were extracted from the solution-annealed hot rolled plate in the transverse direction and prepared according to ASTM E606/E606M-21 for LCF testing (gage length ( $L_0$ ) = 11 mm and gage diameter ( $d_0$ ) = 6 mm), as shown in Fig. 1a. Thermal precharging of H was performed in gaseous H<sub>2</sub> with a pressure of 4.6 MPa at a temperature of 350 °C for 672 h followed by low

Table 1 Chemical composition of as-received AISI 321 in wt.%.

Elements	С	Mn	Si	Cu	Ni	Cr	Ti	Co	N	Fe
Wt.%	0.042	1.801	0.433	0.444	9.012	17.392	0.291	0.146	0.013	Bal

temperature storage at  $-20\,^{\circ}$ C before fatigue test. Hydrogen concentrations were measured using melt extraction by means of Bruker Galileo G8. Thermal pre-charging increased H concentration from 3.5 wt.ppm in the initial state to 21.5 wt.ppm. Strain-controlled LCF testing (strain amplitude is 0.45 %, strain ratio  $R_{\varepsilon}=-1$ ) was performed in-situ at a strain rate of  $1\times10^{-3}$  1/s in H<sub>2</sub> environment with the same pressure of 4.6 MPa at both RT and 120 °C. To protect the extensometer, the test was interrupted when 20 % load drop was observed from the peak stresses recorded during the test, which was denoted as the crack initiation. The number of cycles at this moment was recorded, and the specimens were then fractured in a tensile manner (named as residual fracture in this study, (see Fig. 1b) at temperature close to RT in air. Comparison with as-received material under the same test condition at both temperatures in air was also performed.

The transverse cross-section was used for the initial microstructural characterization. The sample was hot mounted in conductive bakelite resin and ground using P1000, P1200, P2000, P4000 silicon carbide (SiC) abrasive papers on a Struers Tegrapol. This was followed by polishing using diamond suspension of 3  $\mu$ m and 1  $\mu$ m, followed by final polishing with 0.05  $\mu$ m colloidal silica. The initial microstructure of the as-received steel was characterized by Zeiss Gemini 450 scanning electron microscope (SEM) equipped with energy dispersive X-ray spectroscopy (EDS) (Oxford Analysis) and electron backscatter diffraction (EBSD) (Oxford, Symmetry). For post-mortem analysis, fatigue zone from the specimens were identified and marked. Later this region was sectioned using a Buehler Isomet slow speed cutter with a diamond blade along the longitudinal direction. These specimens then directly underwent electrochemical polishing using Struers A3 electrolyte at 26 V for 60 s.

For phase identification and quantification, EBSD measurements were performed on the longitudinal region of the fatigue zone perpendicular to the fracture surface (Fig. 1b) with a step size of  $0.2 \mu m$  covering an area of  $0.3 mm^2$  for statistics. This was in accordance with the suggestion for quantifying phases in heterogenous microstructures of transformation-induced plasticity (TRIP) steels, which is a minimum of  $0.275 mm^2$  with at least 30,000 data points [21]. All measurements were performed at an accelerating voltage of 20 kV with a 12 nA probe current and a working distance of 7-8 mm.

Differentiation and subsequent quantification of DIM from  $\delta$ -ferrite were performed on the EBSD phase maps by "Classify" data analysis mode in AztecCrystal software, where image quality (IQ) maps were used to distinguish martensite and  $\delta$ -ferrite by utilizing band contrast, band slope, and mean angular deviation (MAD) values. The phases were manually selected and distinguished, by protecting zero solutions and austenite phase. This information was stored as a model within the software and then applied across the data set by slight adjustments depending on the quality of IQ maps. The large strain in the mapped area due to deformation-induced martensite lowers the quality of IQ map and thus the confidence of accurate identification, hence the phase quantification should be considered approximate. All EBSD phase maps presented in the study were plotted using open-source MTEX toolbox in MATLAB® [22]. Controlled electron channelling contrast imaging (cECCI) was performed using the backscatter detector in the same SEM, with an operating voltage of 30 kV, probe current of 5 nA and working distance of 8 mm. Two-beam diffraction conditions on a selected grain was achieved using TOCA software [23].

#### 3. Results

#### 3.1. Microstructural observations of as-received steel

The microstructure of as-received AISI 321 in the solution annealed condition along rolling direction (transverse to loading direction) comprised elongated body-centered cubic (BCC) structured  $\delta$ -ferrite and face-centered cubic (FCC) structured Ti(C,N) embedded within the austenitic matrix, as illustrated in Fig. 2.  $\delta$ -ferrite exhibited 'string-like' morphology.

#### 3.2. Fatigue and fractography

Fatigue life in this study was defined as the number of cycles until crack initiation, encompassing both the nucleation and

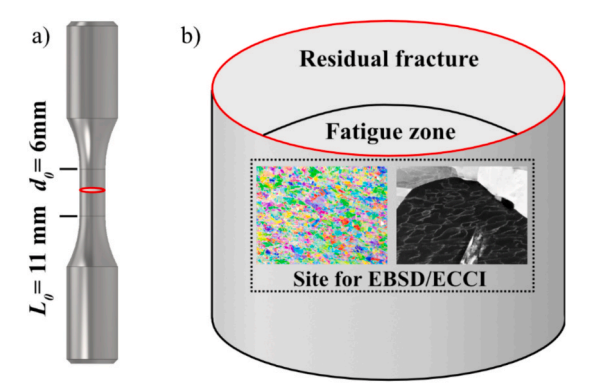


Fig. 1. (a) Geometry and dimensions of low cycle fatigue specimen, all values in mm; (b) Fracture surface denoting fatigue zone, residual fracture zone, and site for EBSD and ECCI measurements.

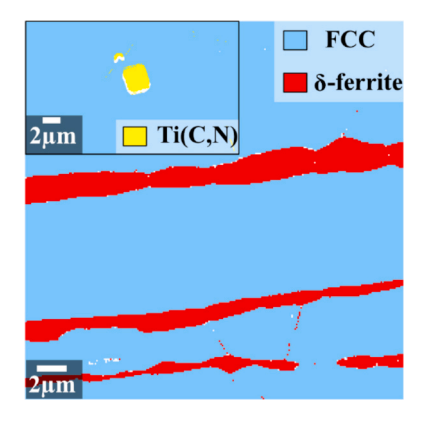


Fig. 2. EBSD phase map of as-received microstructure featuring  $\delta$ -ferrite and Ti(C, N) in austenite.

subsequent propagation of the crack to a critical length that resulted in a measurable load drop (see Section 2 for details). Using the fatigue life in air at RT as a reference, Table 2 presents the normalized difference in the number of cycles to crack initiation between air and  $H_2$  environments at different temperatures. As expected, H uptake reduced fatigue life at room temperature, however a strong reduction in fatigue life was also observed at 120 °C. Additionally, both  $H_2$  and air environments exhibited longer fatigue life at 120 °C compared to room temperature, although the improvement in  $H_2$  was relatively modest.

Fracture surfaces of LCF failed specimens at RT and 120  $^{\circ}$ C were examined to understand the effect of H, as exhibited in Fig. 3 and Fig. 4, respectively. Notice the specimens were fractured in a tensile manner after the initiation of the fatigue crack. The fatigue zone and final fracture area failed by tensile loading after crack initiation are labelled "1" and 'residual fracture' in these figures, respectively. Compared to the specimen tested in the air (Fig. 3a and Fig. 4a), the ones tested in H<sub>2</sub> exhibited a flatter fracture surface perpendicular to the loading direction with nearly parallel secondary cracks in the fatigue zone and residual fracture areas (Fig. 3d, Fig. 3f-g, Fig. 4c and Fig. 4e) at both RT and 120  $^{\circ}$ C.

At RT, in the fatigue zone of specimen tested in air, striations were observed pointing away from the crack initiation site, as marked in Fig. 3b. The dimples in the residual fracture, especially the pull outs of Ti(C,N), denoted the ductile nature of fracture (Fig. 3c) here. In contrast, the fatigue zone of the specimen tested in  $H_2$  at RT exhibited a predominantly striation-free fracture (Fig. 3e-f), though sparsely distributed small areas of striations could be observed occasionally. This fatigue zone featured secondary cracks with surrounding cleavage (Fig. 3f). The difference in the fatigue zone correlates to the drop in LCF performance. To understand the secondary cracks in the fatigue zone, EDX point analyses were performed at bulk and at the crack interface, as shown in Fig. 3h and Fig. 3i. The higher chromium (Cr) and lower nickel (Ni) content at the interface, where cracking occurred, confirmed the presence of  $\delta$ -ferrite. Cracking along the  $\delta$ -ferrite phase boundaries in the fatigue zone, as shown in (Fig. 3f), suggests that such phase boundaries could serve as potential crack initiation and propagation paths during cyclic loading. Additionally, in Fig. 3g, an increase in secondary cracks of the same nature is seen in the residual fracture zone with no dimple formation. Although the residual fracture in tension after the test interruption can also be an indication of the effect of H, it should not be mixed up with the fatigue zone.

At 120 °C, a pronounced drop in life due to H uptake was also found, and there were some changes in the fracture surface characteristics (Fig. 4) compared to RT counterparts (Fig. 3). When tested in air at this temperature, a ductile nature of fracture was seen with fatigue striations in the fatigue zone (Fig. 4b) and dimples in the residual fracture (Fig. 4a). This was like the specimen tested in air at RT. When tested in H<sub>2</sub>, cleavage was observed, and the fatigue zone featured relatively more striation zones compared to the specimen tested at RT (Fig. 3e). Here parallel cracking associated with  $\delta$ -ferrite interphase boundaries was seen as well (Fig. 4d-f). Interestingly, the regions close to  $\delta$ -ferrite interphase boundaries featured fracture without striations (cleavage like) as shown in Fig. 4f. The residual fracture zone was observed with secondary cracks along  $\delta$ -ferrite phase boundaries, as shown in Fig. 4d and Fig. 4g. In this study, no secondary cracks are observed to be associated with grain boundaries of austenite either from fracture surfaces or from cross sections of fatigue zone (Fig. 3e-d, Fig. 4d-f, & Fig. 6b).

#### 3.3. Deformation induced martensite

It has been widely reported that DIM decreases HE resistance of austenitic stainless steel [6,18,19,24,25]. To further understand

**Table 2**Percentage difference in the Number of cycles to crack initiation at 0.45% strain amplitude, relative to test in air at RT.

Environment	Temperature			
	RT	120 °C		
Air	100 %	156 %		
Hydrogen gas	49 %	54.6 %		

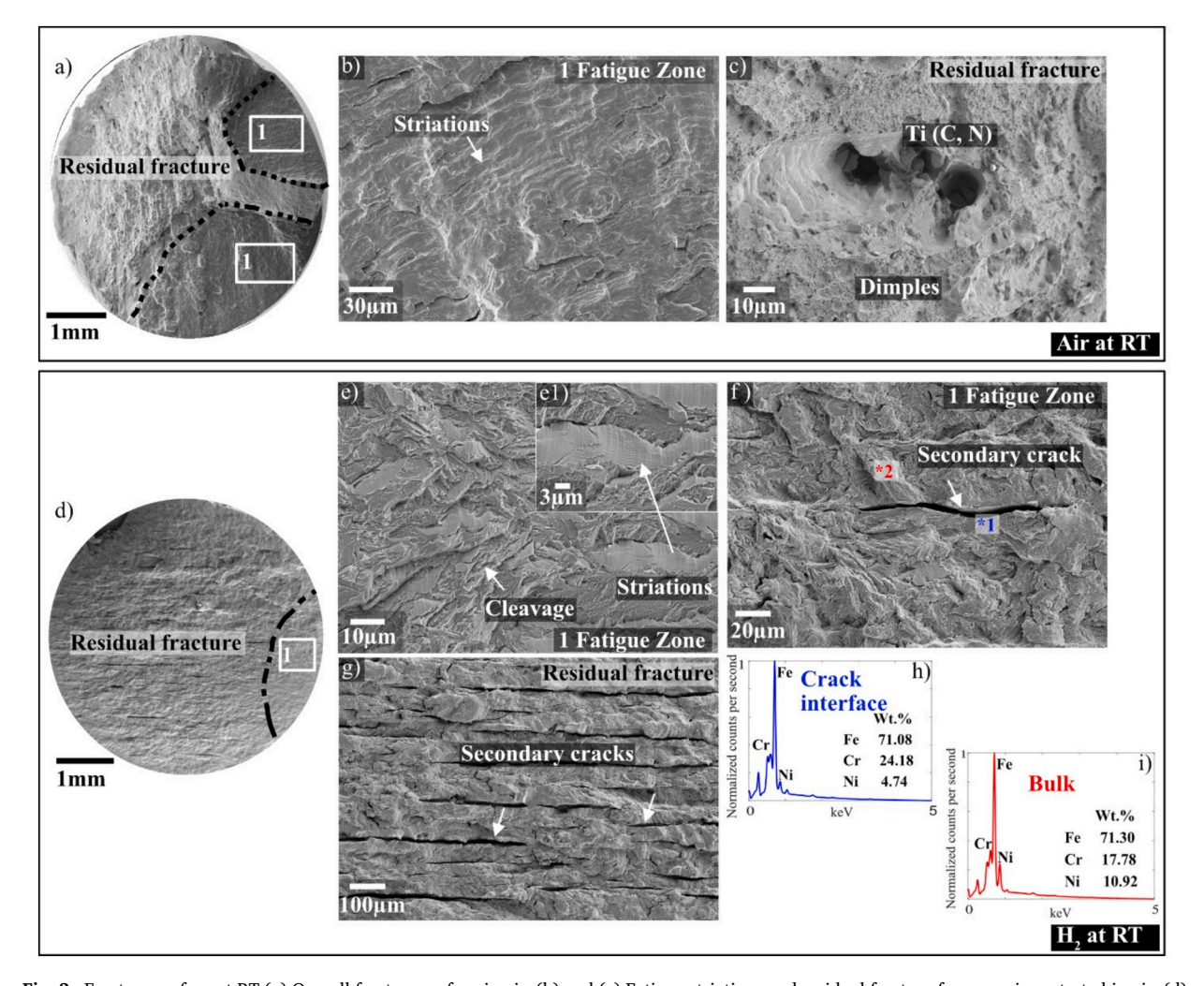
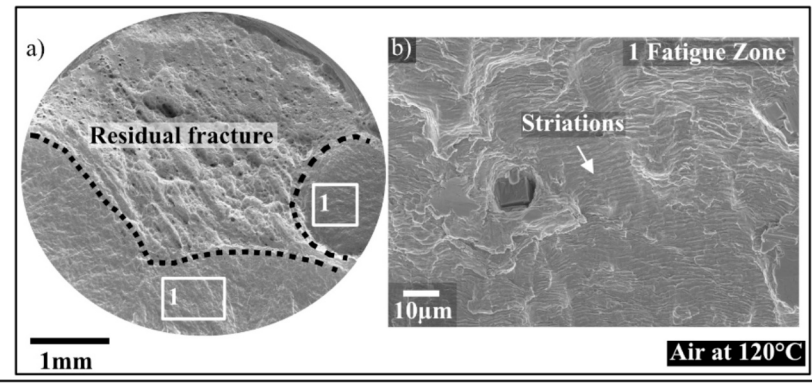


Fig. 3. Fracture surface at RT (a) Overall fracture surface in air; (b) and (c) Fatigue striations and residual fracture from specimen tested in air; (d) Overall fracture surface in  $H_2$ ; (e), (e1) and (f) Cleavage fracture, scarce presence of striations and secondary cracks in fatigue zone of  $H_2$  tested specimens; (g) Secondary cracking in residual fracture; (h-i) EDX point analysis of bulk and near the cracks in fatigue zone of  $H_2$  tested specimens as marked in (f). note: regions marked '1' in (a) and (d) represent fatigue zone.

how this affects HE at varied temperatures in the studied steel, post-mortem analysis of the failed specimens was performed on the longitudinal section of the fatigue zone. EBSD phase map from the tested specimens under different conditions and the schematic location for analysis are exhibited in Fig. 5. Notice DIM and  $\delta$ -ferrite are indistinguishable here and are marked as BCC. The phase fraction of BCC is highest in specimen tested in air at RT, as seen from Fig. 5a. It was known that  $\delta$ -ferrite exhibited 'string-like' morphology, refer to Fig. 2. A large fraction of BCC phase with morphological changes in Fig. 5a is indicative of the presence of martensite. In comparison, testing in gaseous H<sub>2</sub> at RT decreased the fraction of BCC phase considerably, as seen in Fig. 5c. The reduced martensite content was probably due to lower number of cycles to failure (see Table 2). It has been reported that martensite content for a given strain amplitude is linearly correlated to number of cycles in AISI 321 under strain-controlled LCF testing [15]. When tested at 120 °C, the fraction of BCC for samples tested in air and H<sub>2</sub> was like that of  $\delta$ -ferrite in the as-received state, as shown in Fig. 5b and Fig. 5d, suggesting lack of martensite formation at this temperature.

To distinguish martensite from  $\delta$ -ferrite, "Classify" data analysis mode in Aztec Crystal software was used in image quality (IQ) maps. The result is given in Fig. 5e. Deformation-induced martensite was distinguished based on morphology and IQ maps. It typically exhibited lower IQ values, appearing as darker regions. The difference in grain morphology of martensite and  $\delta$ -ferrite further aids in the classification. Compared to martensite, as mentioned earlier, the  $\delta$ -ferrite phase displays a characteristic 'string-like' morphology, often extending across multiple austenite grains aiding in its identification. Notice that Fig. 5e serves as a representative example of the identification technique and not all DIM and  $\delta$ -ferrite regions are explicitly marked in this figure. The amount of DIM can be quantified by image analysis, as presented in Table 3. At room temperature, approximately 31 % DIM was observed in specimens tested in air, whereas  $\sim$  14.7 % was detected in specimens tested in H<sub>2</sub>. At 120 °C, formation of martensite was not observed in either air or H<sub>2</sub> tested specimens, see Fig. 5b, Fig. 5d and Table 3. Under these conditions, the BCC phase detected was  $\delta$ -ferrite, which can be readily



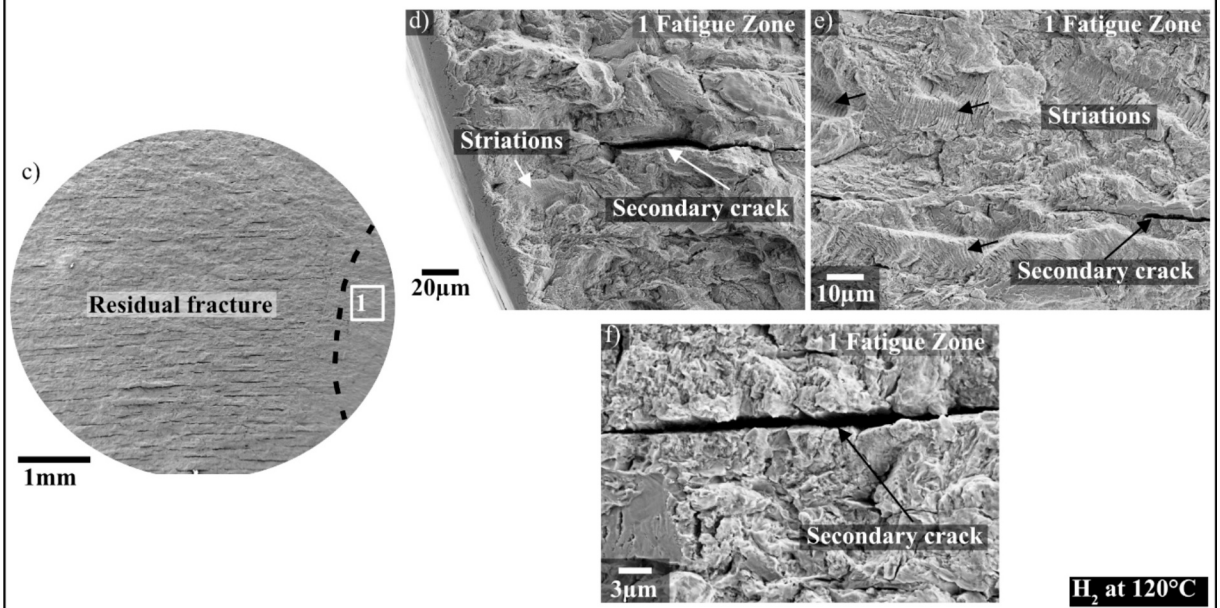


Fig. 4. Fracture surface at 120 °C (a) Overall fracture surface in air; (b) Fatigue striations from specimen tested in air in fatigue zone; (c) Overall fracture surface in  $H_2$ ; (d-e) Presence of striations and secondary cracks along δ-ferrite phase boundaries; (f) lack of striations around δ-ferrite phase boundaries.

distinguished from austenite based on its distinct morphology. These findings confirm that at 120  $^{\circ}$ C and 0.45 % strain amplitude, austenite is stable against DIM formation.

#### 3.4. Strain localization at phase boundaries

It is well known that electron channelling contrast (ECC) is the strongest under two-beam diffraction conditions, enabling observation of crystal defects, such as dislocations, stacking faults, twins in an SEM [23]. At the same locations previously analysed by EBSD in Fig. 5, post-mortem microstructural analysis of specimens tested at 120 °C using controlled-electron channelling contrast imaging (cECCI) is shown in Fig. 6. At 120 °C no DIM formation was observable (see Fig. 5b and Fig. 5d). This indicates that this temperature is above the  $M_{\rm d}$  temperature of the alloy, where DIM formation is not feasible. The deformation is primarily accommodated by slip, as evident from the slip traces observed in austenite irrespective of testing environment in Fig. 6a and Fig. 6b. The presence of  $\delta$ -ferrite is also highlighted in the image.

Controlled-electron channelling contrast imaging can also be used to elaborate the role of  $\delta$ -ferrite interphase. An EBSD phase map, as shown in Fig. 6c, was first acquired near the fatigue zone, as indicated schematically in Fig. 5. Austenite and  $\delta$ -ferrite are the two phases observed here (note: electrochemical polishing removed Ti(C,N) precipitates). Randomly oriented austenite grains with adjacent  $\delta$ -ferrite were selected for detailed analysis, as highlighted in Fig. 6c and its orientation is shown in Fig. 6d. The corresponding cECCI analysis, presented in Fig. 6e, reveals strain localization at the austenite- $\delta$ -ferrite phase boundary, evidenced by regions of increased brightness signifying a higher dislocation density. Additionally, the presence of slip bands and their termination at the  $\delta$ -ferrite phase boundary can be observed in Fig. 6e, highlighting the role of phase boundaries in impeding the dislocation motion.

The strain localization was observed in both samples tested in air and H<sub>2</sub> at 120 °C. A direct comparison to evaluate the influence of

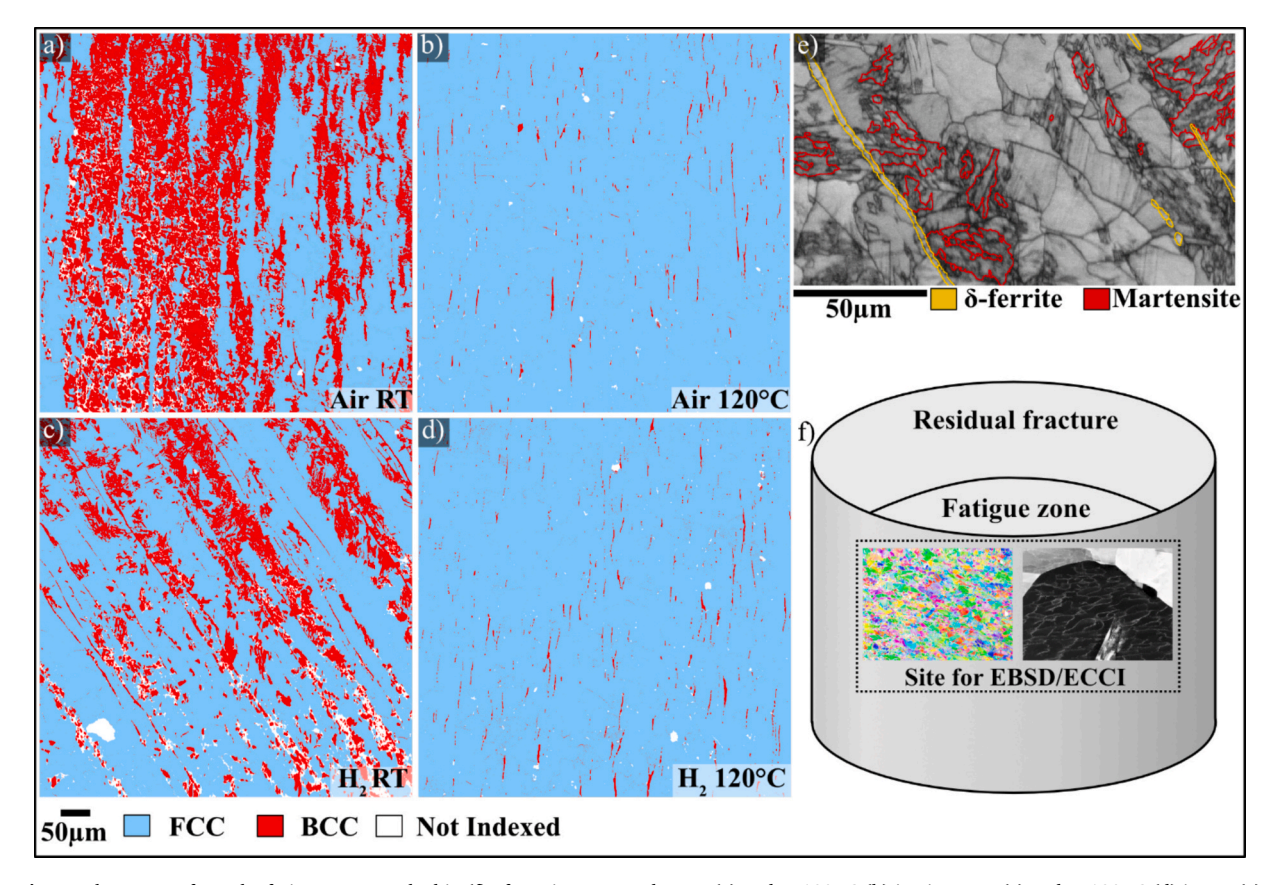


Fig. 5. Phase maps from the fatigue zone marked in (f) of specimens tested at RT (a) and at 120  $^{\circ}$ C (b) in air; at RT (c) and at 120  $^{\circ}$ C (d) in H<sub>2</sub>; (e) Distinguishing  $\delta$ -ferrite and martensite from IQ map with the "Classify" data analysis mode in AztecCrystal software.

H was complicated. Nevertheless, the accumulation of H along the phase boundaries when combined with the strain localization could worsen the interface strength, leading to decohesion of the boundaries. This will be discussed in detail in next section.

#### 4. Discussion

In the literature, hydrogen embrittlement of AISI 321 was often studied by mechanical testing at room temperature on materials with electrochemically charged H. This study investigated the strain-controlled LCF at both room temperature and 120  $^{\circ}$ C in 4.6 MPa gaseous hydrogen atmosphere. It provides insights into the less known HE at elevated temperatures under LCF loading. Compared to room temperature tested specimens in air, a higher number of cycles to crack initiation was observed at an elevated temperature of 120  $^{\circ}$ C. However, it was found that testing in H<sub>2</sub> gas caused a decrease in fatigue "life" at both room temperature and at 120  $^{\circ}$ C.

#### 4.1. Role of phases on HE

In the current study, it was observed that austenite remained stable in specimens tested at 120 °C, with no signs of DIM formation, as shown in Fig. 5b and Fig. 5d. This is attributed to the test temperature being above the  $M_d$  temperature of the alloy [10]. The absence of DIM explains the enhancement in the number of cycles to crack initiation by 56 % in air at 120 °C, compared to room temperature. Similar observations have been made by Grosse et al. [15] who reported that martensite formation follows an exponential decay with increasing LCF testing temperatures in AISI 321. The lack of DIM eliminates its detrimental effect on strain-controlled LCF performance, as martensite formation causes higher cyclic stress response [26].

It is generally accepted that DIM has higher diffusivity and lower solubility of H than austenite, leading to H accumulation at the phase boundaries and accelerating HE. However, despite the absence of DIM transformation at 120 °C, pronounced HE was still observed (Table 2). In comparison to air tested specimen, 65 % drop in life was found at this temperature. The observed drop in fatigue life could be due to the presence of BCC structured  $\delta$ -ferrite having lower solubility and higher diffusivity for H. This is supported by the presence of secondary cracks along  $\delta$ -ferrite phase boundaries in the fatigue zones of specimens tested at both temperatures (Fig. 3f and 4d-f). Similar finding was reported by Bao et al. [15] who stated that  $\delta$ -ferrite accelerates fatigue failure for AISI 304 in H<sub>2</sub> gas at ambient temperature. Its interfaces acted as preferential sites for crack initiation and propagation under both stress-controlled LCF and fatigue crack propagation tests at room temperatures in H<sub>2</sub> due to the accumulation of H there. Unlike DIM,  $\delta$ -ferrite is stable at 120 °C

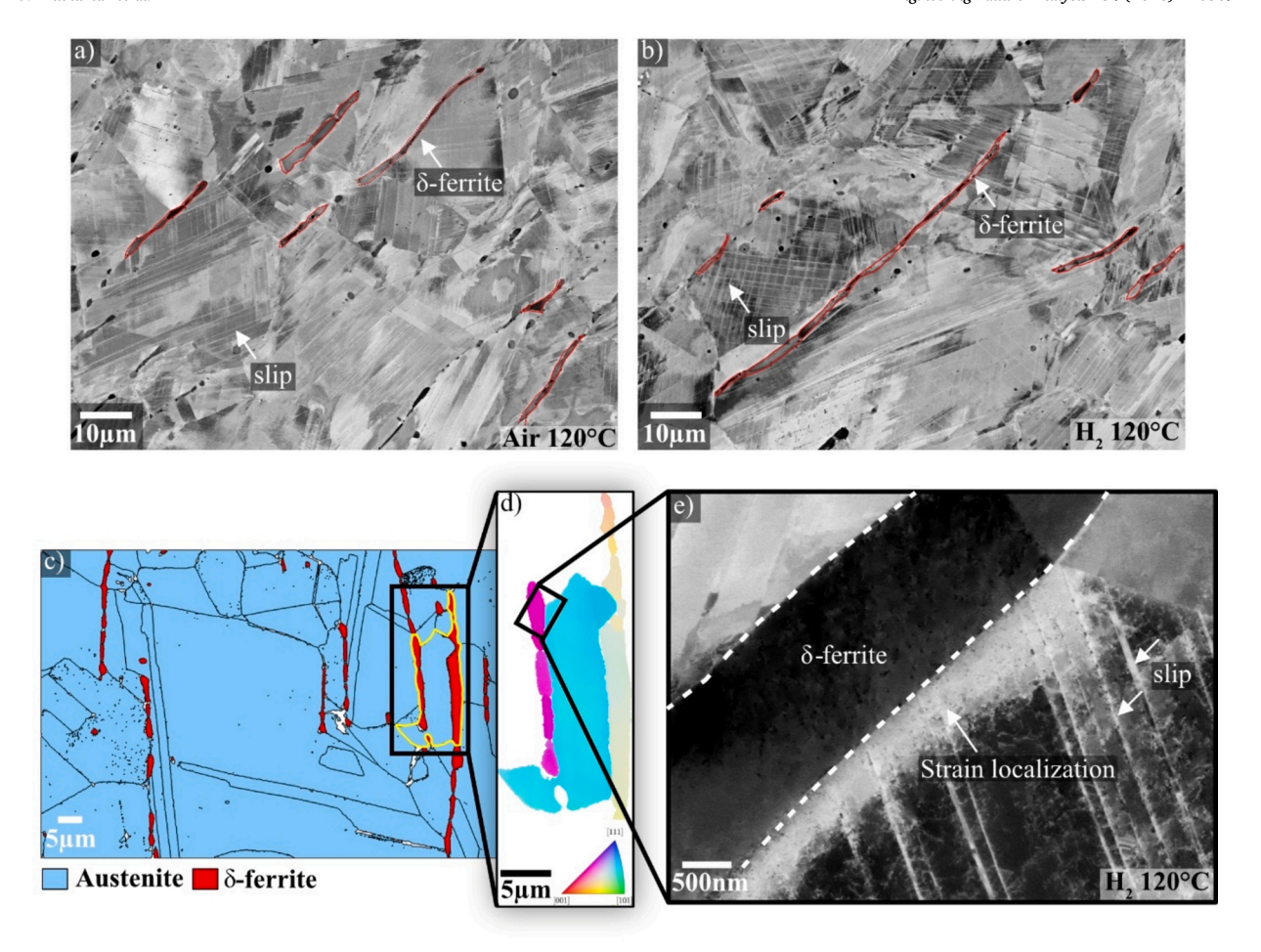


Fig. 6. Deformation of austenite through slip at 120 °C in air (a) and in  $H_2$  (b); (c) EBSD phase map showing the presence of austenite and δ-ferrite; (d) EBSD orientation map of selected grain as highlighted in (c); (e) Image of the same region revealing the strain localization at the austenite-δ-ferrite phase boundary.

 $\begin{tabular}{lll} \textbf{Table 3} \\ \textbf{Amounts of DIM quantified by image analysis after LCF testing at 0.45\% strain amplitude.} \end{tabular}$ 

Environment	Temperature			
	RT	120 °C		
Air	~31 %	nil		
Hydrogen gas	~14.7 %	nil		

and can thus serve as a preferential site for H accumulation, potentially worsening HE at this temperature. The presence of  $\delta$ -ferrite related secondary cracks in specimen tested at 120 °C in H<sub>2</sub> confirms its detrimental role on fatigue life in the absence of DIM. In summary, DIM is detrimental to LCF lifetime with and without H. At 120 °C, a reduced fraction of DIM helped improve the life compared to the room temperature both in air and in H<sub>2</sub>.  $\delta$ -ferrite is also detrimental to HE resistance. Its presence serves as one of the primary roles in inducing HE at the elevated temperature of 120 °C, causing a large drop in life. The governing mechanisms of hydrogen embrittlement responsible for the observed secondary cracking associated with  $\delta$ -ferrite are discussed below.

#### 4.2. Fracture behaviour and HE mechanisms

Two primary mechanisms proposed for HE are hydrogen-enhanced decohesion (HEDE) and hydrogen-enhanced localized plasticity (HELP) [27,28]. In HEDE mechanism, it is suggested that interstitial H lowers cohesive energy between atoms. The accumulation of hydrogen at crack tips, defects, or some microstructural features reduces the critical stress required for atomic separation, leading to brittle fracture by promoting intergranular or transgranular decohesion under stress. On the fracture surface, typical features include

quasi-cleavage, grain boundary fracture and sometimes secondary cracks. On the other hand, the HELP mechanism considers that hydrogen enhances dislocation mobility and localizes plastic deformation at the microscopic level, promoting the formation of microvoids and shear bands, the coalescence of which gives rise to crack initiation and propagation. On the fracture surface, some ductile appearance with evidence of localized plasticity is often revealed.

At room temperature, the fatigue zone of specimens tested in air exhibits typical striations indicative of a ductile behaviour in the alloy (Fig. 3b). However, after prolonged thermal pre-charging (350 °C for 672 h) and subsequent testing in  $H_2$  environment at RT, the fracture surface dramatically changes. Cleavage is the dominant fracture mode (Fig. 3e). Furthermore, the fatigue zone in these  $H_2$  tested specimens shows secondary cracking along  $\delta$ -ferrite interfaces (Fig. 3f). It should be mentioned that a few isolated and sparsely distributed striation zones exist (Fig. 3e1). In addition, slip bands could be observed in some of the untransformed austenite grains from band contrast image of RT  $H_2$  tested specimen shown in Fig. 5e. These features suggest a combination of HEDE and HELP mechanisms. When tested in  $H_2$  at RT, the possible activation of HELP mechanism can lead to highly localized slip deformation transforming austenite into martensite at the crack front. This provides H diffusion pathways that may lead to a local increase in H content [29]. Furthermore, H accumulates at the austenite/martensite interfaces, as newly formed martensite saturates and rejects excess H, promoting preferential crack propagation by weakening the cohesive strength of these boundaries via HEDE [8]. Thus the observed cleavage fracture at RT in  $H_2$  could be in fact a combination of HELP and HEDE mechanisms [30]. Crucially, the observation of secondary cracks along the  $\delta$ -ferrite phase boundaries (Fig. 3f) indicates that these interfaces are prone to H-assisted weakening by a similar mechanism [14]. Accordingly, at RT, the concurrent presence of DIM and  $\delta$ -ferrite correlates with accelerated fatigue crack initiation and propagation via HEDE and HELP mechanisms.

At 120 °C, DIM formation is not favoured. Specimens tested in air exclusively display striations and no indications of brittle behaviour (Fig. 4b). Conversely, specimens tested in H<sub>2</sub> environment exhibits secondary cracks along the δ-ferrite interfaces (Fig. 4d-f). Here fracture mode close to δ-ferrite interface is cleavage (Fig. 4f). Under cyclic loading, crack tip blunting may be inhibited close to these interfaces, and the crack tip may remain relatively sharp. In addition, new cracks could be formed as seen from secondary cracks along these interfaces in the fatigue zone (Fig. 4d-f). Notably, when tested in H<sub>2</sub>, the specimens show more striation-rich regions (Fig. 4e) compared to their RT counterparts (Figs. 3e-e1). The lack of DIM at 120 °C could be the reason for the presence of striations in H<sub>2</sub> tested specimens. Moreover, multiple slipping occurs in austenite in presence of H (Fig. 6b). The combined action of HEDE and HELP mechanisms is thus believed to be responsible for the observed HE at this elevated temperature. Likely, the weight of HELP could be higher than in its RT counterpart. The operative HE processes apparently involve δ-ferrite/austenite phase boundaries. The inherent strain partitioning between  $\delta$ -ferrite and austenite leads to strain localization in austenite (Fig. 6e), with and without the presence of H [31]. Although differences in plastic strain accumulation in these two cases complicate direct comparison of dislocation mobility in austenite, it is known that H promotes dislocation motion through the HELP mechanism [27,28]. Consequently, strain partitioning occurs earlier, accelerating strain localization in austenite at lower LCF cycles. This is confirmed by the extensive slipping in Fig. 6b. Interestingly, as presented in Fig. 6e, slip bands terminate at the  $\delta$ -ferrite phase boundary, indicating impeded dislocation motion there. Meanwhile, a higher dislocation density, evidenced by regions of increased brightness in Fig. 6e, imply dislocation pile up and consequently stress concentration in front of the  $\delta$ -ferrite phase boundary. These interfaces are also preferential sites for H accumulation [32], leading to potential reduction in cohesive strength. The combination of localized increase in interfacial stresses owing to strain localization in austenite (via HELP) and H-induced reduction in interfacial cohesion (via HEDE), could promote faster crack initiation and propagation along  $\delta$  phase boundaries. Nonetheless, the strain localization observed in specimens without the presence of H did not lead to secondary cracking along the phase boundaries (Fig. 4a). Indeed, it is the synergistic effect of hydrogen accumulation and strain localization that lead to secondary cracks and adjacent cleavage-like regions. (Fig. 4f). In summary, at 120 °C in the absence of DIM, our observations are consistent with HELP and HEDE mechanisms acting at  $\delta$ -ferrite/austenite boundaries, which likely contribute to accelerated crack initiation and propagation and reduced LCF life. The presence of δ-ferrite worsens fatigue life, though alternative HE pathways cannot be excluded.

#### 5. Conclusion

This study investigated hydrogen embrittlement in AISI 321 stainless steel using thermal pre-charging and in-situ pressurized low-cycle fatigue testing at room temperature and  $120\,^{\circ}$ C. The results reveal that specimens tested at  $120\,^{\circ}$ C exhibit an extended fatigue life compared to those tested at room temperature in air. This improvement is attributed to the increased austenite stability. Nevertheless, hydrogen embrittlement remains evident at both room temperature and  $120\,^{\circ}$ C. Notably, the absence of martensite at  $120\,^{\circ}$ C does not eliminate embrittlement. The secondary cracking of delta-ferrite boundaries observed in hydrogen could be due to the possible activation of hydrogen-enhanced plasticity (HELP) together with hydrogen-enhanced decohesion (HEDE) and correlates with reduced fatigue life. These findings implicate delta-ferrite interfaces contributes to hydrogen embrittlement. The findings made from our study are crucial for materials selection in hydrogen-powered gas turbines and emphasize the need to minimize the delta-ferrite content to improve hydrogen embrittlement resistance up to  $120\,^{\circ}$ C.

#### CRediT authorship contribution statement

Vishnu Anilkumar: Writing – review & editing, Writing – original draft, Methodology, Investigation, Formal analysis. Stefan Wanjura: Resources, Investigation. Dirk Kulawinski: Writing – review & editing, Resources, Investigation. Frans Palmert: Writing – review & editing, Resources, Investigation. Johan Ahlström: Writing – review & editing, Supervision. Lars Nyborg: Writing – review & editing, Supervision. Yu Cao: Writing – review & editing, Supervision, Funding acquisition, Conceptualization.

#### **Declaration of competing interest**

The authors declare that they have no known competing financial interests or personal relationships that could have appeared to influence the work reported in this paper.

#### Acknowledgements

The authors acknowledge Siemens Energy for the supply of hydrogen gas tested samples and competence centre TechForH2, hosted by Chalmers University of Technology, Sweden and financially supported by the Swedish Energy Agency, Sweden (P2021-90268) and the member companies AB Volvo, Scania CV AB, Siemens Energy AB, GKN Aerospace Sweden AB, PowerCell AB, Oxeon AB, RISE, Stena Rederier AB, Johnson Matthey AB and Insplorion AB.

#### Data availability

The authors do not have permission to share data.

#### References

- [1] E. Stefan, B. Talic, Y. Larring, A. Gruber, T.A. Peters, Materials challenges in hydrogen-fuelled gas turbines, Int. Mater. Rev. 67 (2022) 461–486, https://doi.org/10.1080/09506608.2021.1981706.
- [2] S.M. Kumar, N.S. Shanmugam, Studies on the weldability, mechanical properties and microstructural characterization of activated flux TIG welding of AISI 321 austenitic stainless steel Studies on the weldability, mechanical properties and microstructural characterization of activat, (2018).
- [3] A.I. Mourad, S. Sajith, S. Shitole, A. Almomani, S.H. Khan, A. Elsheikh, A. Kareem, Fatigue life and crack growth prediction of metallic structures: a review, Structures 76 (2025) 109031, https://doi.org/10.1016/j.istruc.2025.109031.
- [4] M. Eichinger, J. Pengg, D. Zwittnig, G. Mori, Hydrogen diffusivity, uptake and embrittlement of solution annealed and cold deformed austenitic stainless steel 1. 4435 at hydrogen pressures up to 1000 bar and 200 o, Corros. Sci. 235 (2024) 112219 https://doi.org/10.1016/j.corsci.2024.112219.
- [5] B. Rafiei, B.M. Sadeghi, B. Mirzakhani, Y. Payandeh, F. Rahimi, Transformation-Induced Plasticity in 304 and 304L Stainless Steels and its effect on Tensile Behavior and Anisotropy, J. Mater. Eng. Perform. (2024) 18–20, https://doi.org/10.1007/s11665-024-09478-4.
- [6] L. Zhang, B. An, S. Fukuyama, T. Iijima, K. Yokogawa, Characterization of hydrogen-induced crack initiation in metastable austenitic stainless steels during deformation, J. Appl. Phys. 108 (2010) 1–5, https://doi.org/10.1063/1.3477321.
- [7] M. Imade, T. Iijima, S. Fukuyama, K. Yokogawa, Effect of Heat-Treatment on High-pressure Hydrogen Gas Embrittlement of Austenitic Stainless Steels, J. Japan Inst. Met. Mater. 72 (2008) 139–145, https://doi.org/10.2320/jinstmet.72.139.
- [8] K.E. Nygren, A. Nagao, P. Sofronis, I.M. Robertson, The Role of Microstructure in Hydrogen-Induced Fatigue failure of 304 Austenitic Stainless Steel, Metall. Mater. Trans. A Phys. Metall. Mater. Sci. 51 (2020) 5704–5714, https://doi.org/10.1007/s11661-020-05977-w.
- [9] Y. Murakami, T. Kanezaki, Y. Mine, S. Matsuoka, Hydrogen embrittlement mechanism in fatigue of austenitic stainless steels, Metall. Mater. Trans. A Phys. Metall. Mater. Sci. 39 A (2008) 1327–1339. DOI: 10.1007/s11661-008-9506-5.
- [10] A. Jain, A. Varshney, A critical review on deformation-induced transformation kinetics of austenitic stainless steels, Mater. Sci. Technol. (united Kingdom) 40 (2024) 75–106, https://doi.org/10.1177/02670836231212618.
- [11] J.A. Lee, Hydrogen Embrittlement. NASA/TM-2016-218602, Shreir's Corros. (2016) 1-62. https://ntrs.nasa.gov/api/citations/20160005654/downloads/20160005654.pdf.
- [12] J.R. Buckley, D. Hardie, The effect of pre-straining and δ-ferrite on the embrittlement of 304L stainless steel by hydrogen, Corros. Sci. 34 (1993) 93–107, https://doi.org/10.1016/0010-938X(93)90261-E.
- [13] C.D. Graham, B.E. Lorenz, Delta ferrite is ubiquitous in type 304 stainless steel: Consequences for magnetic characterization, J. Magn. Magn. Mater. 458 (2018) 15–18, https://doi.org/10.1016/j.jmmm.2018.02.092.
- [14] F. Bao, K. Zhang, Z. Zhou, W. Zhang, X. Cai, L. Zhang, Effect of δ-ferrite on susceptibility to hydrogen embrittlement of 304 austenitic stainless steel in high-pressure hydrogen atmosphere, Anti-Corrosion Methods Mater. 68 (2021) 202–208, https://doi.org/10.1108/ACMM-11-2020-2403.
- [15] M. Grosse, D. Kalkhof, M. Niffenegger, L. Keller, Influencing Parameters on Martensite Transformation during Low Cycle Fatigue for Steel AISI 321 (437) (2006) 109–113, https://doi.org/10.1016/j.msea.2006.04.077.
- [16] A.A. Tiamiyu, A.G. Odeshi, J.A. Szpunar, Deformation and strengthening mechanisms in AISI 321 austenitic stainless steel under both dynamic and quasi-static loading conditions, Miner. Met. Mater. Ser. Part F 6 (2017) 191–202, https://doi.org/10.1007/978-3-319-51493-2 19.
- [17] E. Viyanit, S. Keawkumsai, K. Wongpinkeaw, N. Bunchoo, W. Khonraeng, T. Trachoo, T. Boellinghaus, Hydrogen assisted cracking of an AISI 321 stainless steel seamless pipe exposed to hydrogen-containing hot gas at high pressure, Eng. Fail. Anal. 100 (2019) 288–299, https://doi.org/10.1016/j.engfailanal.2019.02.037.
- [18] X. Xiuqing, A. Junwei, W. Chen, N. Jing, Study on the hydrogen embrittlement susceptibility of AISI 321 stainless steel, Eng. Fail. Anal. 122 (2021) 105212, https://doi.org/10.1016/j.engfailanal.2020.105212.
- [19] C. Huang, W. Cai, L. Qi, Z. Wang, R. Guan, Role of rare-earth yttrium in the hydrogen embrittlement of AISI 321 austenitic stainless steel, Int. J. Hydrogen Energy 47 (2022) 37138–37152, https://doi.org/10.1016/j.ijhydene.2022.08.267.
- [20] P. Rozenak, D. Eliezer, Effects of metallurgical variables on hydrogen embrittlement in AISI type 316, 321 and 347 stainless steels, Mater. Sci. Eng. 61 (1983) 31–41. https://doi.org/10.1016/0025-5416(83)90123-4.
- [21] K. Davut, S. Zaefferer, Statistical reliability of phase fraction determination based on electron backscatter diffraction (EBSD) investigations on the example of an Al-trip steel, Metall. Mater. Trans. A Phys. Metall. Mater. Sci. 41 (2010) 2187–2196, https://doi.org/10.1007/s11661-010-0315-2.
- [22] F. Bachmann, R. Hielscher, H. Schaeben, Texture Analysis with MTEX Free and Open Source Software Toolbox, Solid State Phenom. 160 (2010) 63–68, https://doi.org/10.4028/www.scientific.net/SSP.160.63.
- [23] S. Zaefferer, N.N. Elhami, Theory and application of electron channelling contrast imaging under controlled diffraction conditions, Acta Mater. 75 (2014) 20–50. https://doi.org/10.1016/j.actamat.2014.04.018.
- [24] C. Izawa, S. Wagner, M. Deutges, M. Martín, S. Weber, R. Pargeter, T. Michler, H.H. Uchida, R. Gemma, A. Pundt, Relationship between hydrogen embrittlement and Md30 temperature: Prediction of low-nickel austenitic stainless steel's resistance, Int. J. Hydrogen Energy 44 (2019) 25064–25075, https://doi.org/10.1016/j.ijhvdene.2019.07.179.
- [25] P. Rozenak, Stress induce martensitic transformations in hydrogen embrittlement of austenitic stainless steels, Metall. Mater. Trans. A Phys. Metall. Mater. Sci. 45 (2014) 162–178, https://doi.org/10.1007/s11661-013-1734-7.
- [26] A. Glage, A. Weidner, H. Biermann, Procedia En- gineering effect of austenite stability on the low cycle fatigue behavior and microstructure of high alloyed metastable austenitic cast TRIP- steels, Procedia Eng. 2 (2010) 2085–2094, https://doi.org/10.1016/j.proeng.2010.03.224.
- [27] M.B. Djukic, V. Sijacki Zeravcic, G.M. Bakic, A. Sedmak, B. Rajicic, Hydrogen damage of steels: a case study and hydrogen embrittlement model, Eng. Fail. Anal. 58 (2015) 485–498, https://doi.org/10.1016/j.engfailanal.2015.05.017.

- [28] H. Yu, X. Lu, B. Sun, Y. Ding, M. Koyama, J. He, X. Zhou, A. Oudriss, X. Feaugas, Z. Zhang, Hydrogen embrittlement as a conspicuous material challenge-comprehensive review and future directions, (n.d.). DOI: 10.1021/acs.chemrev.3c00624.
- [29] T. Kanezaki, C. Narazaki, Y. Mine, S. Matsuoka, Y. Murakami, Effects of hydrogen on fatigue crack growth behavior of austenitic stainless steels, Int. J. Hydrogen Energy 33 (2008) 2604–2619, https://doi.org/10.1016/j.ijhydene.2008.02.067.
- [30] Y. Wang, X. Wang, J. Gong, L. Shen, ScienceDirect Hydrogen embrittlement of catholically hydrogen-precharged 304L austenitic stainless steel: effect of plastic pre-strain, Int. J. Hydrogen Energy 39 (2014) 13909–13918, https://doi.org/10.1016/j.ijhydene.2014.04.122.
- [31] D. Lee, B. Sun, S. Lee, D. Ponge, E.A. Jägle, D. Raabe, Comparative study of hydrogen embrittlement resistance between additively and conventionally manufactured austenitic stainless steels, (n.d.).
- [32] D. Choi, J. Nam, B. Moon, S.K. Saha, J. Yoo, J.M. Park, K.H. Yun, N. Kang, Effect of δ–ferrite and strain-induced martensite on hydrogen embrittlement of STS 308 L and STS 316 L all-weld metals, Corros. Sci. 231 (2024) 111977, https://doi.org/10.1016/j.corsci.2024.111977.